Optical coherence and theoretical study of the excitation dynamics of a highly symmetric cyclophane-linked oligophenylenevinylene dimer

Andrew M. Moran
Department of Chemistry, The University of Chicago, Chicago, Illinois 60637

Jeremy B. Maddox
Department of Chemistry, The University of California at Irvine, Irvine, California 92697

Janice W. Hong
Department of Chemistry, The University of California at Santa Barbara, Santa Barbara, California 93106

Jeongho Kim[a] and Rene A. Nome
Department of Chemistry, The University of Chicago, Chicago, Illinois 60637

Guillermo C. Bazan
Department of Chemistry, The University of California at Santa Barbara, Santa Barbara, California 93106

Shaul Mukamel
Department of Chemistry, The University of California at Irvine, Irvine, California 92697

Norbert F. Scherer[b]
Department of Chemistry, The University of Chicago, Chicago, Illinois 60637

(Received 6 January 2006; accepted 22 March 2006; published online 19 May 2006)

Optoelectronic properties of a polyphenylenevinylene-based oligomer and its paracylophane-linked dimer are studied using a variety of experimental and theoretical techniques. Despite the symmetrical structure and redshifted absorption of the dimer versus the monomer, an exciton picture is not the most appropriate. Electronic structure calculations establish changes in charge density upon optical excitation and show localized excitations that cannot be accounted for by a simple Frenkel exciton model. Visible frequency pump-probe anisotropy measurements suggest that the dimer should be considered as a three-level system with a fast, ~130 fs, internal conversion from the higher to lower energy excited electronic state. Signatures of nuclear relaxation processes are compared for electric field-resolved transient grating and two-dimensional photon echo spectra. These measurements reveal that nuclear relaxation occurs on similar time scales for the monomer and dimer. The connection between the spectral phase of four-wave mixing signals and the time dependent width of a nuclear wave packet is discussed. Semiempirical electronic structure and metropolis Monte Carlo calculations show that the dominant line broadening mechanisms for the monomer and dimer are associated with inter-ring torsional coordinates. Together, the theoretical calculations and electric field-resolved four-wave mixing experiments suggest that while the structure of dimer is more rigid than that of monomer, the difference in their rigidities is not sufficient to slow down excited state relaxation of dimer with respect to the monomer. © *2006 American Institute of Physics*. [DOI: 10.1063/1.2196041]

I. INTRODUCTION

Understanding the origin of optoelectronic properties of chromophore aggregates is essential to linking single molecule and macromolecular behavior. In addition to being a fundamental scientific problem, the ability to predict electronic properties of molecular assemblies has important technological implications for designing devices such as ultrafast switches, light-emitting diodes, and photodetectors.[1–7] A continuous change from molecular to bulk properties occurs with an increase of the number of chromophores in an aggregate; intermolecular interactions give rise to collective optical phenomena[8–11] and energy transfer (i.e., band structure). Extensive theoretical and experimental studies of ultrafast dynamics have been made for biological complexes[12–18] and organic polymers.[19–24] These studies provide insight into the manner in which microscopic concepts such as interchromophore distances and orientations determine macromolecular optoelectronic properties. It has long been understood that the interaction-induced resonances for simple dimer systems such as the *J* and *H* aggregates[25,26] are an effect of transition dipole coupling. However, heterogeneity is important for predicting properties of extended materials. For example, it was shown that long-range order enhances the conductivity of organic polymers[27] and charge transport properties of organic transistors.[4,28,29] Therefore, precise synthetic control of aggregate structure is critical to achieve effective control of material function.

[a]Present address: Department of Chemistry, University of Toronto, Toronto, Ontario M5H 3H6, Canada.
[b]Author to whom correspondence should be addressed. Electronic mail: nfschere@uchicago.edu

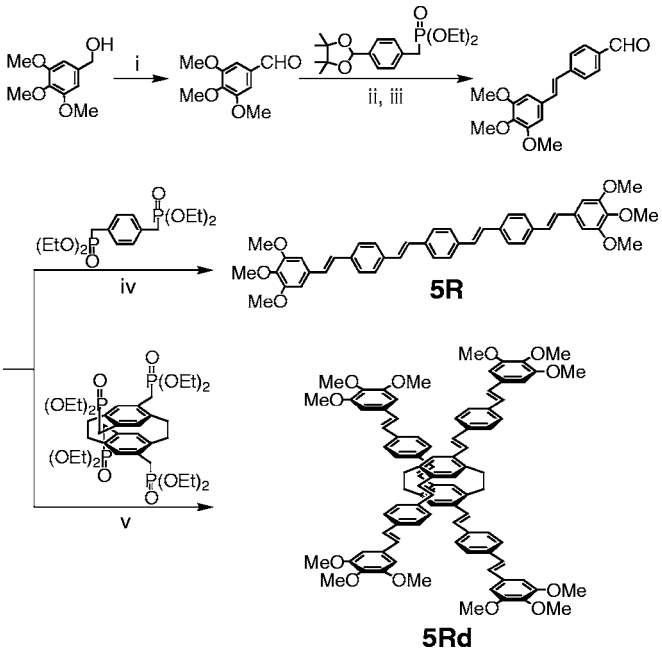

FIG. 1. Syntheses and structures of 5*R* and 5*Rd*. (i) TEMPO, CuCl, O_2, DMF, 15 h. (ii) NaH, toluene, 60 °C, overnight. (iii) 10% HCl, THF, 65 °C, overnight. (iv) KH, THF, 60 °C, overnight. (v) KO*t*-Bu, toluene, 60 °C, overnight.

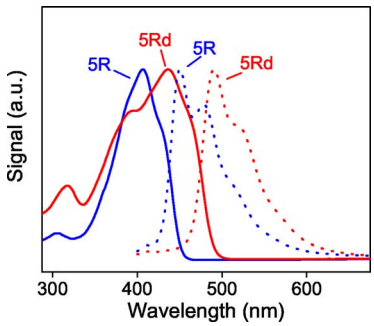

FIG. 2. Absorption (solid) and fluorescence (dotted) spectra of 5*R* (blue) and 5*Rd* (red). The excitation wavelength used to record the fluorescence spectra was 365 nm. Excitation wavelengths from 350–435 nm gave indistinguishable fluorescence spectra.

The class of paracyclophane (PCP) derivatives considered in this paper is well-suited for studying the effects of multichromophore interactions. For example, the dimer (5*Rd*) pictured in Fig. 1 consists of two oligophenylenevinylene (OPV) units held in fixed orientations by covalently binding the 5*R* monomers with a PCP linker.[30–32] Cofacial overlap and close proximity of the phenyl rings in PCP gives rise to strong interactions between the OPV units.[33,34] It has been suggested that this interaction has a significant through-space coupling component (as opposed to through-bond) due to disrupted bond conjugation at the PCP linker.[35–37] The unique electronic structures and well-defined geometries of PCP derivatives have promoted their use as model systems in studies of bonding, ring strain, and π-π^* electron delocalization.[38,39] Synthetic control of the size, orientation, and functionality of the OPV chromophore constituents make these molecules valuable model systems for investigating interchromophore coupling. Furthermore, they are especially suitable for solution-phase spectroscopic study because of their rigid conformations.

Here we present a study of 5*R* and 5*Rd* using a comprehensive set of of nonlinear spectroscopies and electronic structure calculations. The effect of PCP linkage on the absorption spectrum of 5*Rd* is seen in Fig. 2. Multiple transitions are found in the 350–500 nm wavelength range for which a single transition occurs in 5*R*. The spectral dependence of the pump-probe anisotropy for 5*R* and 5*Rd* exhibits differences in the ground-state bleach and excited-state emission responses, which are generally not equivalent as nuclear relaxation in the excited state may be coupled to the anisotropy. Pump-probe (and fluorescence) anisotropy experiments are useful for studying excitation dynamics of systems with multiple electronic levels because the transition dipoles connecting pairs of states may have different orientations in the molecular frame. Therefore, population transfer among various electronic levels is reflected in the polarization dependence of the signals. Pump-probe techniques are particularly useful in this regard since time-resolved fluorescence anisotropy experiments do not give information on the ground-state bleach. Calculated transition densities of the hole and particle are plotted in real space to reveal the localized nature of the excitations contributing to experimental anisotropy signals. In addition, we compare signatures of static line broadening in electric field-resolved transient grating and photon-echo spectra. The coordinates responsible for spectral inhomogeneity are identified based on semiempirical Hamiltonians and a metropolis Monte Carlo (MMC) sampling algorithm. Jonas and co-workers performed similar experiments on the cyanine dyes IR144 and HDITCP and thoroughly investigated the manifestation of solvation dynamics in spectral features using a Ti:sapphire laser (~800 nm).[40] It was recently shown that the phase-stability needed to implement these techniques at visible wavelengths could be achieved using diffractive optics.[41,42] Our experiments are performed at the shortest wavelength yet reported for the two-dimensional Fourier transform electronic spectroscopy (405 nm).

The results of a recent article involving similar PCP derivatives are relevant to the present paper.[43] This work is a comparative study of a monomer and two dimers (linked by PCP) in which resonance Raman and fluorescence measurements are used to investigate the nature of the states underlying the broad absorption band of the dimer. The resonance Raman excitation spectra suggest that the higher-energy shoulder of the dimer (similar to the linear spectrum of 5*Rd*, see Fig. 2) represents an additional electronic state. Fluorescence anisotropies of the dimers are sensitive to the excitation frequency and also point to the presence of at least one additional blueshifted electronic state for both dimers. These results provide similar information to the pump-probe anisotropy experiments reported here. In addition, the relative contributions of homogeneous and static line broadening to the absorption bands of the monomer and two related dimers were determined by the resonance Raman intensity analysis. These measurements show that the monomer has a narrower

homogeneous line width than the dimers. Our electric field-resolved experiments are sensitive to the same line broadening mechanisms.

The collective electronic oscillators (CEO) analysis is useful for understanding aggregation effects on the real-space origin of the optical response.[44] Predictions were made for the photophysics of distyrylbenzene-substituted dimers using a scheme consisting of distinct "phane" (localized on PCP) and "monomeric" (localized on the monomer constituents) excitations. In this model, emission was predicted to occur from the lower energy monomeric state and therefore internal conversion should not follow photoexcitation into this band. Initial population of the higher-energy phane state was not explicitly considered, but internal conversion should be anticipated in this situation.[45] In the present work, we use a semiempirical treatment for the electronic structure of 5*R* and 5*Rd* to characterize the ground- and excited-state potential energy surfaces. We divide the chromophores into smaller stilbenoid units and characterize the ground- and excited-state molecular properties of these tractable pieces. Metropolis Monte Carlo sampling of the molecular configuration space gives insight into the origin of inhomogeneous broadening in the electronic spectra of the monomer and dimer complexes.

The measurements and calculations presented here have broader implications for understanding the effects of intermolecular interactions on the electronic structures of molecular assemblies. The fundamental issue for understanding the electronic structure of 5*Rd* (and other coupled molecular systems) is the description of interactions between the 5*R* subgroups. If this coupling is weak (i.e., through-space electrostatic coupling), then the Frenkel exciton model,[46,47] which is outlined in Appendix A, may be used to describe the electronic states of 5*Rd* with a basis of 5*R* substates. However, the Frenkel exciton model is not valid for systems in which the electronic orbitals of its monomers overlap (i.e., through-bond coupling). For homodimers, such as 5*Rd*, the transition dipoles between the ground-state and the two single exciton states are predicted to be perpendicular by the Frenkel exciton model. Therefore, the appropriate physical picture may be experimentally identified with anisotropy measurements.

In the next section, we describe the synthetic, spectroscopic, and computational methods used in this work. Results and discussion are presented in Sec. III. Finally, the main conclusions of this work are summarized in Sec. IV.

II. EXPERIMENT

A. Synthesis

All chemicals were ordered from Aldrich and used as received. ^{1}H and ^{13}C NMR spectra were recorded on a Varian Inova 400 NMR. Mass spectrometry was performed by the UC Santa Barbara Mass Spectrometry Lab. Syntheses of 1-(diethylphosphonatemethyl)-4-(4′,4′,5′,5′-tetramethyl-1′,3′-dioxolan-2′-yl)benzene,[33] 1,4-bis-(diethylphosphonatemethyl)benzene,[48] and 4,7,12,15-tetrakis-(diethylphosphonatemethyl)[2.2]paracyclophane[35] have been previously reported. All reactions were carried out in the exclusion of O_2 and water unless otherwise specified. A schematic of the synthesis is shown in Fig. 1.

3,4,5-Trimethoxybenzaldehyde. A 500 mL round bottomed flask was charged with 3,4,5-trimethoxybenzyl alchohol (10.2 g,51.5 mmol), 2,2,6,6-tetramethylpipiridine 1-oxyl (TEMPO) (1.06 g,5.07 mmol), copper(I)chloride (0.52 g,5.3 mmol), and DMF (250 mL). O_2 was bubbled through the solution for 15 h. The resulting solution was concentrated under reduced pressure, extracted with diethyl ether, and washed with brine. Drying over anhydrous magnesium sulfate and evaporation yielded 9.4 g (93%) of the product as pale pink plates. ^{1}H-NMR (400 MHz,$CDCl_3$) δ: 9.886 (*s*,1H) 7.145 (*s*,2H) and 3.952 (*s*,9H). ^{13}C-NMR (100 MHz,$CDCl_3$) δ: 191.31, 153.85, 131.91, 106.88, 56.48. HRMS (EI): m/z=196.0735 (M^+), Δ=0.3 ppm.

1-(4′,4′,5′,5′-Tetramethyl-1′,3′-dioxolan-2′-yl)-4-(3″,4″,5″-trimethoxystyryl)benzene. A three-necked 100 mL round bottomed flask was charged with 3,4,5-trimethoxybenzaldehyde (1.48 g,7.55 mmol) and 1-(diethylphosphonatemethyl)-4-(4′,4′,5′,5′-tetramethyl-1′,3′-dioxolan-2′-yl)benzene (3.11 g,87.4 mmol). Dry toluene (30 mL) was vacuum transferred into this flask. Upon cooling the flask to 0 °C, NaH was added and the mixture was allowed to warm to room temperature and then heated to 60 °C overnight. The resulting solution was concentrated under reduced pressure, extracted with dichloromethane and washed with brine. Drying over anhydrous magnesium sulfate and evaporation gave 3.0 g (99%) of a pale yellow powder. ^{1}H-NMR (400 MHz, $CDCl_3$), δ: 7.512 (*d*, J=8.8 Hz, 2H), 7.492 (*d*, J=8.8 Hz, 2H), 7.049 (*d*, J=16.4 Hz, 1H), 7.021 (*d*, J=16.4 Hz, 1H), 6.749 (*s*, 2H), 5.998 (*s*, 1H), 3.930 (*s*, 6H), and 3.879 (*s*, 3H). ^{13}C-NMR (100 MHz, $CDCl_3$), δ: 153.58, 139.24, 137.76, 133.23, 129.05, 128.08, 126.87, 126.56, 103.70, 99.91, 82.92, 61.19, 56.31, 24.56, and 22.41. HRMS (EI): m/z=398.2098 (M^+), Δ=1.3 ppm.

4-(3′,4′,5′-Trimethoxystyryl)benzaldehyde. A solution of 1-(4′,4′,5′,5′-tetramethyl-1′,3′-dioxolan-2'-yl)-4-(3″,4″,5″-trimethoxystyryl)benzene (3.0 g, 7.53 mmol) in 1.2 M HCl (150 mL) and THF (75 mL) was heated to 65 °C for 12 h, open to air. The resulting solution was concentrated under reduced pressure, extracted with dichloromethane and washed with brine. Drying over anhydrous magnesium sulfate and evaporation gave the crude product, which was purified by silica gel chromatography (dichloromethane) to afford 2.2 g (98%) of the product as a pale yellow powder. ^{1}H-NMR (400 MHz, $CDCl_3$) δ: 10.002 (*s*, 1H), 7.880 (*d*, J=8.4 Hz, 2H), 7.658 (*d*, J=8.4 Hz, 2H), 7.201 (*d*, J=16.4 Hz, 1H), 7.057 (*d*, J=16.4 Hz, 1H), 6.782 (*s*, 2H), 3.937 (*s*, 6H), and 3.893 (*s*, 3H). ^{13}C-NMR (100 MHz, $CDCl_3$) δ: 191.67, 153.52, 143.39, 138.67, 135.29, 132.32, 132.20, 130.31, 126.87, 126.79, 104.03, 61.06, and 56.20. HRMS (EI): m/z=248.1216 (M^+), Δ=3.7 ppm.

1,4-bis[4′-(3″,4″,5″-Trimethoxystyryl)styryl]benzene (5*R*). A 100 mL round bottomed flask was charged with 4-(3′,4′,5′-trimethoxystyryl)benzaldehyde (502 mg, 1.68 mmol) and 1,4-bis-(diethylphosphonatemethyl)benzene (202 mg, 0.53 mmol) into which dry THF (50 mL) was vacuum transferred. Upon cooling the flask to 0 °C, KH was added and the mixture allowed to warm to room temperature

and then heated to 60 °C overnight. Over the course of the reaction, a finely divided yellow precipitate formed. This precipitate was collected by filtration, dissolved in dichloromethane, and washed with brine. The solvent was evaporated to yield 215 mg (60%) of compound 5*R* as a pale yellow powder. ^{1}H-NMR (400 MHz, CD_2Cl_2) δ: 7.557 (*s*, 2H), 7.550 (*d*, J=8.8 Hz, 2H), 7.539 (*d*, J=8.8 Hz, 2H), 7.172 (*s*, 2H), 7.092 (*d*, J=16.4 Hz, 1H), 7.058 (*d*, J=16.4 Hz, 1H), 6.774 (*s*, 2H), 3.897 (*s*, 6H), and 3.791 (*s*, 3H). 13C-NMR (100 MHz, CD_2Cl_2) δ: 154.12, 137.31, 137.25, 133.51, 129.09, 128.66, 128.60, 128.04, 127.43, 127.30, 104.15, 61.08, 56.59, and 30.24. HRMS (EI): m/z=666.3003 (M^+), Δ=3.3 ppm.

4,7,12,15-tetrakis(4′-[3″,4″,5″-Trimethoxystyryl]styryl)-[2.2] paracyclophane (5*Rd*). A 100 mL round bottomed flask was charged with 4-(3′,4′,5′-trimethoxystyryl)benzaldehyde (665 mg, 2.60 mm) and 4,7,12,15-tetrakis-(diethylphosphonatemethyl)[2.2]paracyclophane (300 mg, 0.37 mmol). Dry toluene (30 mL) was vacuum transferred into this flask. The reaction flask was cooled to 0 °C and a solution of KO*t*-Bu (365 mg, 3.25 mmol) in dry THF (15 mL) was added dropwise. The mixture was allowed to warm to room temperature and then heated to 60 °C overnight. The resulting mixture was diluted with dichloromethane and washed with brine. The organic phase was dried over $MgSO_4$ and filtered. After removal of the solvent, the crude product was purified by silica gel chromatography (hexanes:chloroform: ethyl acetate (1:4:1)) to yield compound 5*Rd* (80%) as a yellow-orange powder. ^{1}H-NMR (400 MHz, CD_2Cl_2) δ: 7.624 (*d*, J=8.4 Hz, 2H), 7.523 (*d*, J=8.4 Hz, 2H), 7.286 (*d*, J=16 Hz, 1H), 7.141 (*d*, J=16 Hz, 1H), 7.122 (*d*, J=16 Hz, 1H), 7.050 (*s*, 1H), 6.959 (*d*, J=16 Hz, 1H), 3.916 (*S*, 6H), and 3.805 (*S*, 3H). ^{13}C-NMR (100 MHz, CD_2Cl_2) δ: 154.12, 138.67, 138.65, 137.58, 137.35, 137.25, 133.52, 129.09, 128.81, 128.67, 128.09, 127.63, 127.32, 125.72, 104.08, 93.05, 61.10, and 56.57. LRMS (FAB): m/z=1386 (M^+).

B. Spectroscopy

Degenerate frequency pump-probe experiments were performed with the high-rep rate (100 kHz), low dispersion laser system described in Ref. 49. Two-color pump-probe measurements were made using a homebuilt 2 kHz amplified Ti:sapphire laser system, which produces 50 fs, 50 μJ pulses centered at 800 nm. The laser is an upgraded version of the system described in Ref. 50, the oscillator is now cavity dumped;[51] the mirrors surrounding the Ti:sapphire gain medium in the amplifier were replaced with 25 and 12.5 cm (CVI) focal length dielectric mirrors; higher-efficiency 1200 g/mm gratings (Spectrogon) were installed in the stretcher and compressor. In all measurements, the pump beam was obtained by second-harmonic generation (SHG) in a 200-μm-thick Type-I beta barium borate (BBO) crystal (Quantum Technology). A tunable probe beam is produced with an optical parametric amplifier (OPA) (measurements made using a white light continuum had an order of magnitude lower signal to noise). In the first stage of the OPA, a Type-I $KNBO_3$ crystal is used to amplify the near IR portion of a continuum made by focusing ~1 μJ of the 800 nm beam into a 2 mm sapphire disk. The amplified near IR portion of the continuum is then combined with the residual 800 nm pulse to give 10–50 nJ, 80–90 fs pulses tunable from 450–520 nm. The transparency range of $KNBO_3$ allows for more efficient production of 450–480 nm pulses than a near-IR-seeded all-BBO design; this property is also useful for efficient mid-infrared pulse generation in the 3 μm region.[50,52] The pump and probe were compressed and precompensated for material dispersion from transmissive optics in the pump-probe setup by retroreflecting the beams through separate prism pairs. In the degenerate pump-probe experiments performed with the high rep-rate laser system, the pump (~1 nJ) and probe (<0.1 nJ) were focused into the sample with 150 and 100 mm focal length lenses, respectively. A 30 cm focal length spherical mirror and 20 cm focal length achromatic lens were used to focus the pump (100 nJ) and probe (~5 nJ) pulses in the two-color experiments (2 kHz laser system). For all pump-probe anisotropy experiments, the sample was contained in a spinning cell rotated at 10 Hz and had a 0.2 mm path length.

Transient anisotropy data were acquired by orienting a polarizer (Karl Lambrecht, MGTYA-5) in the probe beam at 45° with respect to the pump polarization. Parallel and perpendicular polarization components of the probe (with respect to the pump polarization) were separated after the sample by a Rochon polarizer (Karl Lambrecht, MRA-10) and both polarizations were detected simultaneously with two identical Si photodetectors (New Focus, Nirvana 2007). Signals were processed with two lock-in amplifiers (Stanford Research, SR-830) referenced to a chopper in the pump beam and sampled 1000 times at each delay step with a 16-bit ADC (National Instruments). Scans were repeated ten times and averaged. The probe signal was divided by that of the reference to give $\Delta T/T$, the fractional change of the transmitted probe intensity induced by the pump pulse. This signal detection scheme resulted in better than one part in 10^6 sensitivity. The instrument response function was measured with CCl_4 in the optical Kerr effect geometry before and after data acquisition to ensure that there was no shift in the time delay. The temporal instrument response for the 400 nm–400 nm pump-probe experiments was 60 fs, whereas the two-color experiments had a time resolution of 100–130 fs due to material dispersion in the OPA and group-velocity mismatch in the sample.

Absorptive and dispersive contributions to the transient grating (TG) and photon echo signals were obtained by spectral interferometry.[53–56] The diffractive optic (DO)-based interferometer shown in Fig. 3 is designed to minimize the phase drift between two pairs of pulses: pulses 1 and 2 (pump); pulse 3 (probe) and local oscillator. Each pair is derived from the ±1 diffraction orders of a laser pulse incident on the DO (Holoeye Photonics) to give a rectangular pattern, which is then imaged onto the sample. This particular design has also been effective for the implementation of a novel six-wave mixing technique.[57,58] The parabolic mirrors in this setup (Edmund, 17.5 in. focal lengths) are used in an on-axis geometry to minimize astigmatism as well as spheri-

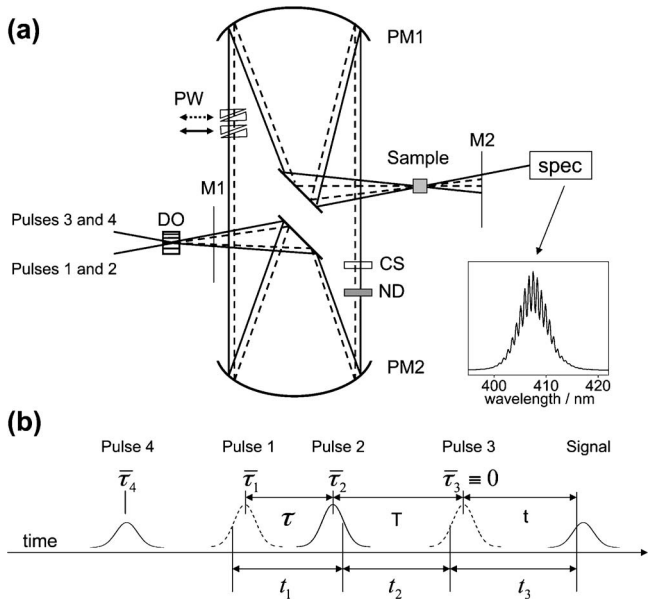

FIG. 3. (a) Setup used for heterodyned transient grating and photon echo measurements. Two distinct pulse-pairs are created with the diffractive optic (DO): pulses 1 and 2 (pump); pulse 3 (probe) and pulse 4 (local oscillator). Solid and dashed lines represent displacement in the dimension orthogonal to the figure plane (i.e., height in the laboratory). The use of parabolic mirrors (PM1 and PM2, 17.5 in. focal lengths) ensures well-defined phase fronts at the sample. The delay τ is varied by translating prism wedges (PW) in the paths of pulses 1 and 2. Masks spatially isolate the ±1 diffraction order beams (M1) and the collinear signal and LO after the sample (M2), which interfere in a spectrometer (spec) to give an interference spectrum (shown as an inset). The local oscillator is attenuated using a neutral density filter (ND). Pulse 3 is delayed with respect to the local oscillator using glass cover slips ($\bar{\tau}_4=-700$ fs). (b) General four-wave mixing pulse sequence. Arrival times of the pulses (at their peaks) are represented by $\{\bar{\tau}_i\}$. The delays, $\tau=\bar{\tau}_2-\bar{\tau}_1$ and $T=\bar{\tau}_3-\bar{\tau}_2$, are experimentally controlled. Intervals between field-matter interaction times are given by t_1, t_2, and t_3.

cal and chromatic aberrations. The heterodyne-detected signal phase is insensitive to ubiquitous vibrations of the optics because all beams are directed to the sample using common mirrors. Measurement of the phase drift for this interferometer gives a standard deviation of 0.14 radians over 4 hours with 400 nm pulses, which compares well to the phase stability of interferometers reported by others.[41,42] The four-wave mixing signals and local oscillator pulses, which are made collinear after the sample, are focused into a 0.32 m monochromator (Jobin-Yvon TRIAX 320) and dispersed with 600 g/mm grating (blazed at 450 nm) on a charge coupled device array detector (Hamamatsu S7032-1007). The absolute phase of the signal is calibrated by measuring the transient grating signal from a transparent solvent (dispersive signal) without moving the sample cell. Pulse energies for beams 1 and 2 are both 40 nJ, whereas beam 3 was 10 nJ. The local oscillator is attenuated by three to four orders of magnitude with a neutral density filter and precedes the probe by ~700 fs. The full width at half maximum (FWHM) spot size of each beam at the sample is ~125 μm. The sample is contained in a flow cell with a 1 mm path length (OD=0.3) for the TG and photon echo measurements.

In the TG technique, the delay between the two grating forming beams, τ, is set equal to zero and the signal spectra and phases are obtained while the delay T is scanned (see Fig. 3). The present experiments differ from recently reported electronically resonant optical heterodyned TG measurements[59,60] in that spectral interferometry rather than the single channel detection and phase cycling is implemented to completely characterize the signal field. We will show that additional information is obtained this way.

Photon echo experiments require varying the delay, τ. Furthermore, τ must be varied with interferometric precision (we use a 0.67 fs step size at 400 nm) to compute a two-dimensional correlation spectrum by Fourier transformation with respect to τ. This delay is scanned using the method recently introduced by Brixner *et al.*[61] A pair of prism wedges (Edmund, 3 mm thick and 1° wedge angle) at conjugate orientations is inserted into the path of each grating forming beam. Translation of one wedge with respect to the other changes the material path length of the pulse without changing the alignment, thus varying the arrival time at the sample. This method is highly effective because the linear stage (Melles Griot Nanomover) moves with high precision (<50 nm step size with 100 nm repeatability) for the step sizes used in the experiment. In our setup, 1 mm wedge translation gives a delay of ~37 fs and therefore the delay precision is about 3.7 as. The interference spectrum is measured while τ is scanned (positive and negative values) and the delay T is fixed. Dispersed detection of the signal gives an effective Fourier transform with respect to t; the time-domain data is numerically transformed with respect to τ at every directly detected frequency component, ω_t, to give the two-dimensional (2D) correlation spectrum. We use the data processing algorithm presented in Ref. 41 to compute 2D spectra.

III. RESULTS AND DISCUSSION

A. Electronic structure models

We have performed a series of semiempirical quantum chemistry calculations. The Austin model 1 (AM1) method of Dewar *et al.*[62] is used to model ground-state molecular geometries and energies, whereas electronic transitions are characterized using Zerner's reparametrization of the intermediate neglect of differential overlap model for spectroscopy (INDO/S or ZINDO).[63] All electronic structure calculations are performed using the GAUSSIAN 03 quantum chemistry package.[64]

Figure 4(a) compares the experimental and theoretical absorption spectra for the AM1 minimum energy ground-state structure of 5*R*. The wavelengths and oscillator strengths of the singlet electronic transitions predicted by ZINDO are shown as vertical red lines. We have included an overall redshift of 600 cm^{-1} for the computed spectra to compensate for ZINDO's overestimation of the transition energies. States labeled II-IV are identified according to the scheme used by Wang *et al.* in Ref. 31. The theoretical line shape for the monomer was generated from 25 transitions using the static (Gaussian) limit of the overdamped Brownian oscillator model where we have assumed a line broadening parameter of $\Delta=1400$ cm^{-1} for each transition.[65] Apart from the vibronic features in the main absorption band (II), the AM1/ZINDO calculation and the Brownian oscillator

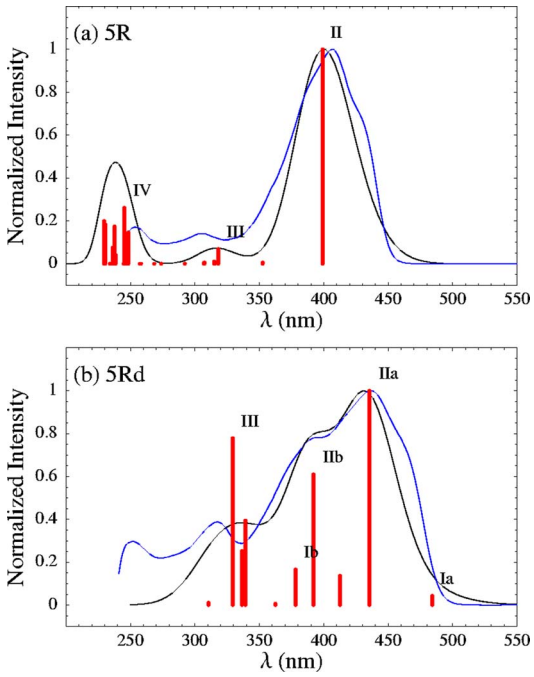

FIG. 4. Comparison of (blue) experimental and (black) theoretical line shapes for (a) 5*R* and (b) 5*Rd*. The theoretical curves were obtained by fitting the line-shape parameters of an overdamped Brownian oscillator model using transition frequencies and transition dipoles from ZINDO calculations. The dominant electronic transitions are labeled by numbers and red lines indicate the wavelengths and relative oscillator strengths of the ZINDO transitions.

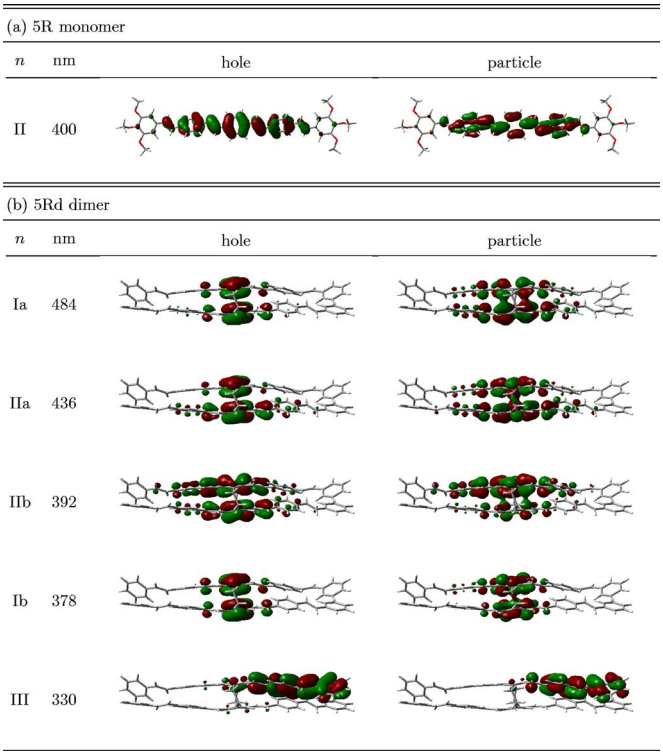

FIG. 5. Selected natural transition orbitals for (a) the AM1 minimum energy structure of 5*R* and (b) the relaxed AM1 5*Rd* structure derived from x-ray crystallographic data.

model provide a reasonable representation for the electronic spectrum of the monomer.

For the dimer, the ZINDO spectrum obtained with the AM1 minimum energy 5*Rd* structure did not agree well with the experiment. We constructed the 5*Rd* structure from x-ray crystallographic data of the 3*Rd* molecule[35] shown in Fig. 6(d). This was accomplished by appending a second styrl group to each arm of the molecule, although terminal methoxy groups were not added. A constrained AM1 optimization was performed with the PCP moiety frozen. Figure 4(b) shows the ten lowest energy singlet transitions (redshifted by 600 cm^{-1}) for the x-ray derived 5*Rd* structure. Again, the theoretical line shape was obtained by varying the line widths of the transitions. A satisfactory fit to the experimental data was obtained using $\Delta=1100$ cm^{-1} for the six lowest energy transitions and $\Delta=2750$ cm^{-1} for the four remaining higher energy transitions. The larger Δ value for the higher energy transitions was necessary in order to compensate for the rather large oscillator strength of state III. The present calculations predict that Ia is the lowest energy singlet while the previous work[31] based on x-ray diffraction data for a different distryl-benzene PCP molecule[30] reported that the lowest energy ZINDO transition is IIa.

To further characterize the nature of the monomer and dimer's excited states we analyzed the hole-particle components of the transition density matrices in the natural transition orbital (NTO) representation.[66] This provides a three-dimensional (3D) real space visualization of the excited hole-particle pair. The hole-particle NTO's for state II of 5*R* are shown in Fig. 5(a). Even though the geometry is nonplanar, the particle and hole show significant delocalization across most of the molecule due to the large contributions from the conjugated π orbitals of the carbon backbone. The NTO's for selected transitions of 5*Rd* are shown in Fig. 5(b). The hole and particle are highly localized on the PCP core for transitions to states Ia and Ib, whereas III is localized on one of the distryl groups. Transitions to states IIa and IIb represent the dominant contributions to the absorption spectrum between 375–500 nm since these two states have the largest oscillator strengths. These transitions are best characterized as something between a "phane" and "monomer" excitations because there are significant contributions from both the PCP core and the innermost styrl groups.

To trace the origin of the inhomogeneous broadening, we have analyzed the influence of low frequency torsional rotations on the optical transition frequencies and used a MMC algorithm[67] to partially sample the molecular configuration space. The 5*R* monomer is dissected into smaller more tractable pieces. The smallest component we consider is the *trans*-stilbene molecule. For stilbene and *PPV* oligomers in general, there is some difficulty in determining the precise minimum energy conformation. Discrepancies of molecular planarity between experiment and calculations (and between different levels of theory) stem from the flat potential energy surface (PES) for torsional rotation about C–C single bonds joining the phenyl and vinyl groups.[68] We performed a 2D (36×36 points) AM1 PES scan as a function of dihedral angle rotation, ϕ and ϕ', about the C–C single bonds connecting the vinyl group to the phenyl rings. All other coordinates were allowed to completely relax at each point. A ZINDO calculation was performed to calculate the electronic

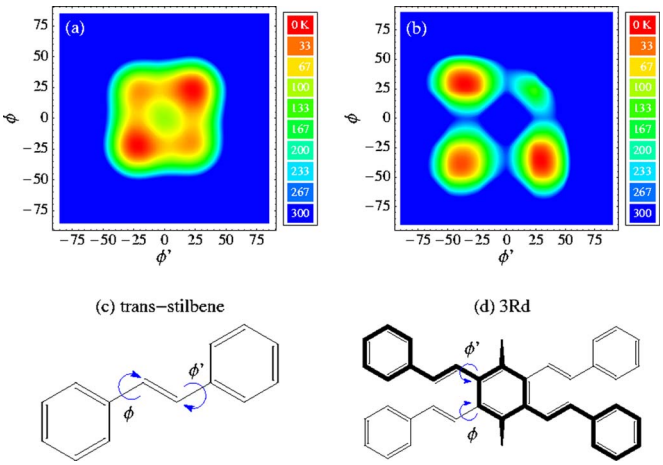

FIG. 6. Contour plots of the AM1 ground state potential energy surfaces as a function of dihedral rotation about C–C single bonds for (a) trans-stilbene and (b) 3*Rd*. For reference, we have included a cutoff energy of 208 cm^{-1} indicated by the contour formed by the blue background. The dihedral angles ϕ and ϕ' used to construct the potential energy surfaces are illustrated schematically with blue arrows in the molecular structures for (c) stilbene and (d) 3*Rd*.

transition frequencies and oscillator strengths at each scan point. The PES of the excited states were given by the sum of the ground-state energy and the corresponding optical transition frequency.

Figure 6(a) shows the AM1 PES for the ground state of stilbene. In Fig. 6(c), the dihedral coordinates involved in the potential scan are identified with blue arrows in the molecular diagram of stilbene. The ground state exhibits four stable local minima; the two most stable local minima of the ground state correspond to nonplanar C_i configurations with dihedral angles $\phi=\phi'=\pm 21°$. For reference, the contour formed by the blue background is equivalent to the thermal energy at 300 K (208 cm^{-1}). The barrier heights between different conformers in the ground state are very low (<70 cm^{-1}), so that at ambient temperatures, the Boltzmann distribution of conformers is very broad. We expect that the dihedral angles of 5*Rd* involving the C–C single bonds that join the PCP core to the styrl arm are constrained due to the steric effects originating from the overlap of charge densities associated with different styrl groups. Figure 6(b) shows the PES's for a 2D AM1 potential energy scan (15×15 points) for the distyrlbenzene dimer 3*Rd*. These coordinates are indicated by blue arrows in the top-side view diagram of 3*Rd* in Fig. 6(d), where the bold-faced lines represent elevation above the plane. The blue background again corresponds to a cutoff energy of 208 cm^{-1}. There are several local minima and the barriers for transitions among the stable conformers are large compared to *trans*-stilbene, so that the ground state Boltzmann distribution of molecular configurations is more tightly packed around the local minima. The two degenerate off-diagonal potential minima $(\phi,\phi')=(-36,29)=(29,-36)$ are the most stable and correspond to the vinyl groups pointing in the same directions. The on-diagonal wells centered at $(\phi,\phi')=(24,24)$ and $(\phi,\phi')=(-38,-38)$ correspond to the vinyl groups pointing away and towards each other, respectively, with the latter being more energetically favorable.

B. Steady state spectra

Absorption and fluorescence emission spectra of the monomer and dimer are shown in Fig. 2. The absorption spectra of 5*R* and 5*Rd* are similar except for the presence of a higher-energy shoulder (390 nm) for the dimer. The resonant Raman excitation spectra for similar monomer and PCP dimer systems suggest this feature represents an additional electronic state.[43] The lower-energy portions of the absorption bands and the fluorescence spectra possess similar vibronic line shapes. This suggests that the lowest energy transition of the dimer is not localized on the PCP moiety. In support of this view, emission from the monomeric state (localized on the aromatic styrl arms of 5*Rd*) of the dimer is consistent with results for other distyrylbenzene compounds.[30] We assign the higher-energy shoulder of the absorption band for 5*Rd* (390 nm) to an excitation localized on PCP and the lower-energy portion of the band (435 nm) to a monomeric state(s).

Transition IIa corresponds to the monomeric emitting state of 5*Rd*. Significant transition density is computed for both the styrl arms and PCP core (Fig. 5), which represents mixing between the PCP and monomeric substates. As discussed in the previous section, mixing between these substates is also computed for transition IIb. However, the transition density of IIb is more localized to the PCP core than that of IIa, with IIa exhibiting greater charge redistribution on the stryl arms (i.e., monomeric character). This aspect of the calculation is consistent with experiments for similar PCP dimers. Resonance Raman measurements for similar dimers show that vibrational modes localized on the PCP moiety have greater intensities for excitation of transition IIb, whereas the ethylenic stretching modes local to the styrl arms have more intensity when the excitation wavelength is tuned to transition IIa.[43]

C. Pump-probe anisotropy

Degenerate frequency pump-probe data and transient anisotropies for 5*R* and 5*Rd* are shown in Fig. 7. The transient transmission of the probe polarization component parallel to the pump polarization, S_{ZZZZ}, show a rapidly decaying (nearly instantaneous) spike at time zero and changes little on the 100 ps time scale due to the long-lived excited states (~2 ns) (Ref. 30) and slow orientational diffusion of these large molecules. For both molecules, the perpendicular (to the pump) probe polarization component, S_{ZZXX}, is smaller in magnitude and has a similar profile to the S_{ZZZZ} data except for the lack of a sharp spike at time zero. The polarization dependence is interpreted by computing the anisotropy

$$r(T)=\frac{S_{ZZZZ}(T)-S_{ZZXX}(T)}{S_{ZZZZ}(T)+2S_{ZZXX}(T)}. \quad (1)$$

The transient anisotropy of 5*R* at time zero is ~0.42 and decays to ~0.32 in 100 ps, whereas that of 5*Rd* decays from ~0.4 to ~0.16 in the first picosecond. The difference in anisotropies at $T=0$ is not sufficient to suggest an additional molecular process; experimental precision is 0.01–0.02 an-

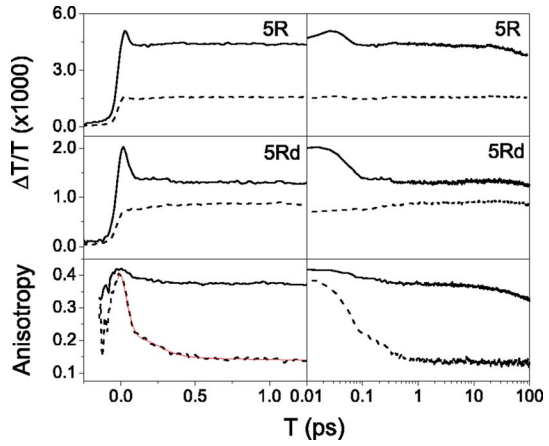

FIG. 7. Degenerate (400 nm) transient probe transmission for 5*R* (top) and 5*Rd* (middle) measured parallel (solid) and perpendicular (dashed) to the pump polarization. Short (linear) and long (log) time scales are plotted in the left and right columns, respectively. Bottom left: Transient anisotropy [Eq. (1)] for 5*R* (black solid) and 5*Rd* (dashed). The solid red line represents a fit to the transient anisotropy of 5*Rd* using Eq. (2). Bottom right: Transient anisotropy for 5*R* (black solid) and 5*Rd* (dashed) on a longer time scale.

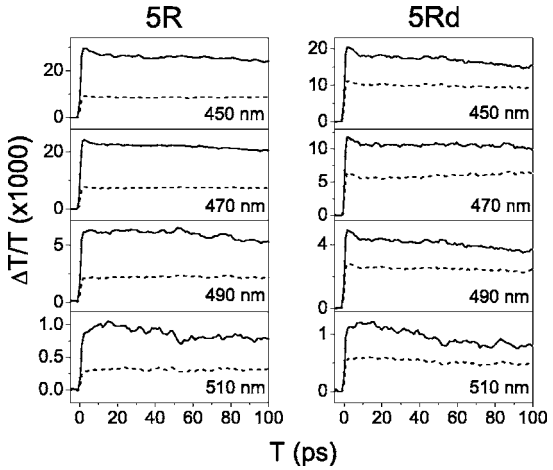

FIG. 8. Transient probe transmission for 5*R* (left) and 5*Rd* (right) measured parallel (solid) and perpendicular (dashed) to the pump polarization. The pump wavelength is 400 nm for all data and the probe wavelength is indicated in each panel.

isotropy units. The anisotropy decay for 5*Rd* was fit with the function

$$r(T) = a_1 \exp\left[\frac{-4\ln 2(T-T_0)^2}{t_g^2}\right] + a_2 e^{(-T/\tau_1)}\cos[2\pi(\omega T+\phi)] + a_3 e^{(-T/\tau_2)} + b. \quad (2)$$

The best fit is given (up to 4 ps) by a Gaussian of t_g =400 fs width, an exponentially damped (τ_1=50 fs) cosine function with a 120 cm^{-1} frequency and phase of 40°, and a τ_2=1 ps exponential decay to an offset of b=0.133. The values of a_1, a_2, and a_3 are 0.086, 0.195, and 0.029, respectively. The fit is displayed in the lower left panel of Fig. 7. It is believed that the 120 cm^{-1} frequency oscillation does not reflect electronic coupling of the monomers because of its low amplitude and subperiod decay. Rather this low-frequency vibration probably affects the orientation of the electronic transition moment.[69] The fast decay in the one-color anisotropy profile of the dimer could be interpreted as an effect of either adiabatic (nuclear relaxation) or nonadiabatic (internal conversion) relaxation. The one-color experiment gives no information on the excited molecules once they leave the phase space defined by the probe spectrum. Thus, population dynamics on a time scale greater than ~1 ps cannot be extracted from the degenerate frequency measurement. Experiments with a tunable probe are useful for identifying the correct process.

Two-color pump-probe results for 5*R* and 5*Rd* are presented in Fig. 8. Anisotropies for all probe frequencies are shown in Fig. 9. The most obvious difference in the degenerate and two-color results is that the two-color S_{ZZZZ} data do not exhibit a sharp feature at time zero. Measurements for the monomer are consistent with expectations for a two-level system in solution: the initial value is ~0.4 and only the effect of solute reorientation is seen on the 100 ps time scale at all probe wavelengths. However, results for the dimer reveal more complicated dynamics. Figure 7 (bottom left) shows that at times less than ~800 fs, both the ground-state bleach (GSB) and excited state emission (ESE) contribute to the anisotropy, whereas at delay times greater than 800 fs the signal is dominated by the GSB. This interpretation is based on the fact that the GSB anisotropy has weak time dependence for processes that are not associated with solute reorientation.[70] In addition, the contribution from ESE vanishes when molecules in the excited state undergo nuclear relaxation and leave the phase space defined by the spectrum of the probe pulse. Therefore, the one-color anisotropy at delay times greater than ~800 fs may be used to compute the angles between transition dipoles for 5*Rd* in the ground state. Linear combinations of the fundamental orientational averages given in Appendix B are used to calculate anisotropies for arbitrary angles between the transition dipoles of 5*Rd*. The dimer is treated as a three-level system because our data does not show strong evidence of excited-state absorption (ΔT is positive and the magnitude is consistent with only GSB and ESE contributions). For the GSB, the *ZZZZ* and *ZZXX* contributions from the four diagrams given in Fig. 10(a) are summed to give the tensor elements

$$S_{ZZZZ}(T=T') = 1/5 + 1/5\cos(\theta)^2 + 1/15\sin(\theta)^2, \quad (3a)$$

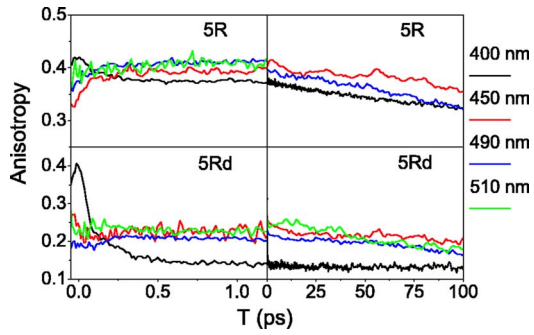

FIG. 9. Transient anisotropy, Eq. (1), for 5*R* (top) and 5*Rd* (bottom). The pump wavelength for all data is 400 nm and the various probe wavelengths are indicated by the line colors given in the figure legend. Short and long time scales are shown in the left and right panels, respectively.

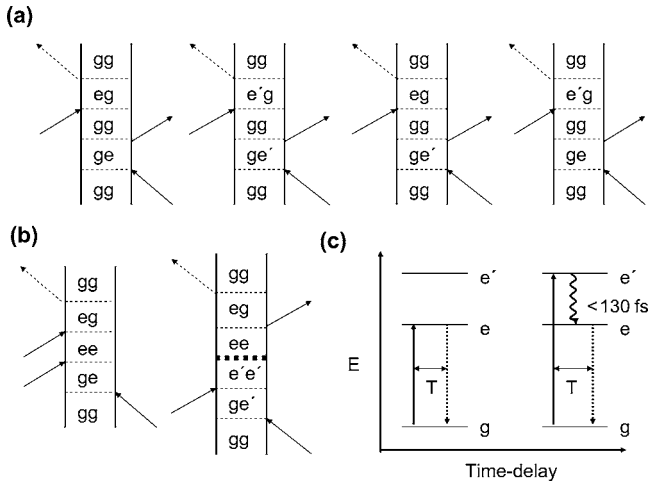

FIG. 10. (a) Double-sided Feynman diagrams corresponding to GSB of a three-level system. These diagrams represent the degenerate pump-probe measurements for 5*Rd*. Time increases from bottom to top. Interactions from the right (left) are with the bra (ket). (b) Double-sided Feynman diagrams for ESE of a three-level system. These diagrams represent the two-color pump-probe measurements for 5*Rd*. The bold dashed line in the diagram on the right denotes a population transfer occurring during the delay between the pump and probe pulses. (c) Energy level representations of the Feynman diagrams shown in panel (b). Solid and dashed lines represent interactions with the pump and probe, respectively. The squiggly line in the diagram on the right represents a population transfer, which is bounded by <130 fs. The energy levels e and e' correspond the calculated states IIa and IIb (see Sec. III A), respectively.

$$S_{ZZXX}(T=T') = 1/15 + 1/15\cos(\theta)^2 + 2/15\sin(\theta)^2, \quad (3b)$$

where T' denotes a single population time such that the orientations of the transition dipoles connecting states e and e' to the ground state (μ_{eg} and $\mu_{e'g}$) are fixed. Here, it is assumed that $|\mu_{eg}| = |\mu_{e'g}|$. An angle of about 60° is consistent with our measurements.

The two-color anisotropies of 5*Rd* have an initial value of 0.20–0.23 and decay on the time scale of solute reorientation at all probe wavelengths from 450–520 nm (pump is 400 nm), which suggests that internal conversion between the higher (e') and lower energy (e) excited states occurs within the time resolution of our 2 kHz rep-rate laser system (100–130 fs). The angle between the transition dipoles, $\mu_{e'g}$ and μ_{eg}, may also be calculated using the two-color results. Similar to the calculation of GSB anisotropy, the diagrams in Fig. 10(b) are used to calculate the ESE anisotropy. The angle dependence of the anisotropy is also given by Eq. (3). A discrepancy of about 10° is found compared to the prediction made using the GSB (the difference is clearly seen in Fig. 9). It is possible that the charge distribution of the excited states changes with nuclear relaxation and/or that there are more than three levels. Spontaneous emission measurements for similar systems show no evidence of more than three levels and give a similar anisotropy of ~0.2 for excitation at ~400 nm.[43]

Interesting dynamics in pump-probe and fluorescence anisotropies have been observed[17,18,71–74] and predicted[70,75,76] for coupled molecular systems. In these studies, dephasing of a coherent superposition of excited states prepared by the pump pulse is manifested in a fast (subpicosecond) anisotropy decay. The dynamics may be further complicated by contributions from excited state absorption. However, we do not see evidence of coherent effects in our data, most likely because the bandwidth of the pump pulse (~250 cm^{-1}) is narrow compared to the energy gap of several thousand wave numbers (cm^{-1}) between the IIa and IIb excited states of 5*Rd*.

D. Electric field-resolved transient grating and photon echo

The fundamental observable in heterodyne-detected four-wave mixing is the signal field, $E_S^{(3)}(t,T,\tau)$, which under perfect phase-matching conditions is related to the third-order polarization by[65]

$$E_S^{(3)}(t,T,\tau) = \frac{i2\pi l\omega_t}{n(\omega_t)c}P^{(3)}(t,T,\tau), \quad (4)$$

where $n(\omega_t)$ is the sample's refractive index, l is the sample length, c is the speed of light and T and τ represent the experimentally controlled pulse delays. The electric field for a sequence of four laser pulses [Fig. 3(b)] may be written as

$$E(\mathbf{r},\tau) = \sum_{j=1}^{4}[E_j(\mathbf{k}_j,\tau) + E_j^*(\mathbf{k}_j,\tau)], \quad (5)$$

where

$$E_j(\mathbf{k}_j,\tau) = \epsilon_j(\tau-\bar{\tau}_j)\exp[i\mathbf{k}_j\mathbf{r} - i\bar{\omega}_j\tau - i\phi_j(\tau)]. \quad (6)$$

In Eq. (6), $\epsilon_j(\tau-\bar{\tau}_j)$ is a slowly varying envelope function for pulse j centered at time $\bar{\tau}_j$ with carrier frequency $\bar{\omega}_j$, wave vector $\mathbf{k}_j$, and the temporal phase function $\phi_j(\tau)$. The frequency domain electric field, $\tilde{E}_j(\mathbf{r},\omega)$, is given by

$$\tilde{E}_j(\mathbf{k}_j,\omega) = \int_{-\infty}^{\infty} d\tau E_j(\mathbf{k}_j,\tau)\exp(-i\omega\tau), \quad (7)$$

where $\tilde{E}_j(\mathbf{k}_j,\omega)$ is centered at $\omega=0$ because $E_j(\mathbf{k}_j,\tau)$ is complex. We choose to shift $\tilde{E}_j(\mathbf{k}_j,\omega)$ by $\bar{\omega}_j$ so that the frequency domain electric fields given in this paper, $E_j(\mathbf{k}_j,\omega)$, are centered at their actual frequencies, $\bar{\omega}_j$. This convention is often used to represent the complex electric fields of coherent light pulses.[77] We define the frequency domain electric field by

$$E_j(\mathbf{k}_j,\omega) = \xi_j(\omega)\exp[i\mathbf{k}_j\mathbf{r} + i\varphi_j(\omega)], \quad (8)$$

where $\varphi_j(\omega)$ is the spectral phase and $\xi_j(\omega)$ is the real spectral amplitude. With the above definitions for the electric field, the phase-matched component of the polarization ($\mathbf{k}_s = -\mathbf{k}_1+\mathbf{k}_2+\mathbf{k}_3$) is expressed as a convolution of the material response function and the laser pulses by

$$P^{(3)}(\mathbf{k}_s,t,T,\tau) = \int_0^{\infty}dt_3\int_0^{\infty}dt_2\int_0^{\infty}dt_1 S^{(3)}(t_3,t_2,t_1) \times E_3(\mathbf{k}_3,t-t_3)E_2(\mathbf{k}_2,t-t_3-t_2) \times E_1^*(\mathbf{k}_1,t-t_3-t_2-t_1), \quad (9)$$

where t_i represent time intervals between the four field-matter interactions [see Fig. 3(b)]. The form of the third-order impulse response function, $S^{(3)}(t_3,t_2,t_1)$, has been discussed in detail.[65] Signals for other choices of $\mathbf{k}_s$ are

obtained by changing E_j to E_j^* as appropriate.

The spectral amplitudes and phases of the four-wave mixing signal fields are obtained by spectral interferometry.[53–56] We define the total heterodyne-detected interference spectrum, $I_{\mathrm{tot}}(\omega_t,T,\tau)$, by[77–79]

$$I_{\mathrm{tot}}(\omega_t,T,\tau,\bar{\tau}_4)=\left|\int_{-\infty}^{\infty}dt[E_S^{(3)}(t,T,\tau)+E_4(t-\bar{\tau}_4)]\exp(i\omega_t t)\right|^2, \tag{10}$$

where $E_S^{(3)}(t,T,\tau)$ is defined in Eq. (4) and parametric dependence on the signal wave vector, $\mathbf{k}_s$, has been suppressed. After filtering the signal and local oscillator intensities by Fourier transform methods,[53] the complex cross term of Eq. (10) may be written as[61]

$$I_{\mathrm{het}}[\omega_t,T,\tau,\bar{\tau}_4;\psi(\omega_t)]=\hat{\xi}_S(\omega_t,T,\tau)\hat{\xi}_4(\omega_t)\exp\{i[\psi(\omega_t)-\omega_t\bar{\tau}_4]\}, \tag{11}$$

where $\hat{\xi}_j(\omega_t,T,\tau)=\xi_j(\omega_t,T,\tau)\exp[i\mathbf{k}_j\mathbf{r}t]$ and $\psi(\omega_t)$ is the phase difference between the signal and local oscillator, $\psi(\omega_t)=\varphi_S(\omega_t)-\varphi_4(\omega_t)$. Equation (10) assumes that the instrument response is uniform for all frequencies within the bandwidths of the local oscillator and signal pulses. The delay, $\bar{\tau}_4$, is obtained by Fourier transforming an interference spectrum of pulse 3 and the local oscillator. The power spectrum of the local oscillator, $|\xi_4(\omega_t)|^2$, is measured by blocking pulses 1–3 in our experimental apparatus [Fig. 3(a)]. The phase of the local oscillator, $\varphi_4(\omega_t)$, is calibrated by performing a heterodyned transient grating experiment with neat chloroform. Chloroform is transparent at 405 nm and therefore the signal is dominated by a dispersive component [i.e., $\varphi_s(\omega_t)=\pi/2,3\pi/2$].[60] Dividing Eq. (11) by $\hat{\xi}_4(\omega_t)$ and $\exp(-i\omega_t\bar{\tau}_4)$, then subtracting $\varphi_4(\omega_t)$ from $\psi(\omega_t)$ gives the heterodyne detected signal field,

$$E_S^{(3)}(\omega_t,T,\tau)=\hat{\xi}_S(\omega_t,T,\tau)\exp[-i\varphi_S(\omega_t)]. \tag{12}$$

The real part of $E_S^{(3)}(\omega_t,T,\tau)$ is absorptive and the imaginary component is dispersive.

Field-resolved TG measurements for the monomer and dimer are presented in Fig. 11. This measurement is a special case of Equation (12) in which $\tau=0$. The heterodyned wavelength-resolved signal is expressed as

$$E_{\mathrm{WRTG}}^{(3)}(\omega_t,T,\tau=0)=E_S^{(3)}(\omega_t,T,\tau=0). \tag{13}$$

The T dependence of the absorptive TG spectra resembles the frequency-integrated pump-probe measurement (Fig. 7), which is expected since pump-probe and TG are given by the same slice of Eq. (12) ($\tau=0$ fs and T is varied). Distinct T-dependent spectral features are seen in the dispersive TG signal. At $T=0$ fs, the sign of the signal is, respectively, negative and positive for the low and high frequency portions of the signal spectrum. For both 5*R* and 5*Rd*, this feature disappears by $T\approx 50$ fs and the dispersive signal spectrum becomes completely positive. The delay of signal emission with respect to the center of pulse 3 is the primary origin of this feature. The signal emission times are given by the slopes of the spectral phases, which are presented in the bottom row of Fig. 11 at various population times. In addition, the curvature of the spectral phase shows that the signal possesses a slight positive chirp with lower frequencies emitted at earlier times t.

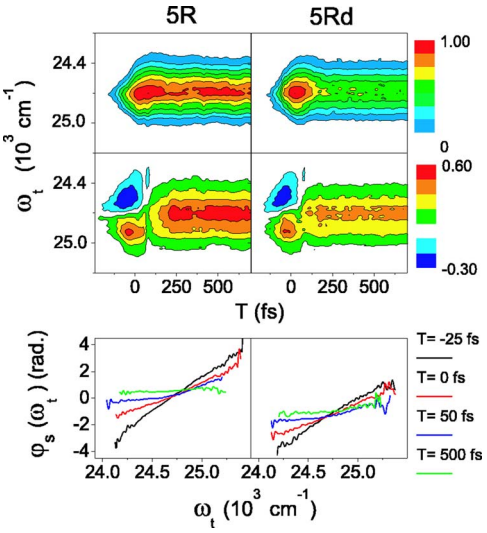

FIG. 11. Absorptive (top row) and dispersive (middle row) transient grating signals for 5*R* (left) and 5*Rd* (right). The absorptive and dispersive spectra are defined by the real and imaginary parts of Eq. (13), respectively. The relative intensity is indicated in the figure legend. These data are not deconvoluted for the finite temporal duration of the laser pulses. Spectral phases of the signal fields for 5*R* (left) and 5*Rd* (right) at four values of the pump-probe delay, T, are presented in the bottom row.

The spectrogram is an intuitive representation of the signal field and may be computed using[77,80]

$$\Sigma(\omega_t,t)=\left|\int_{-\infty}^{\infty}d\tau E(\tau)g(t-\tau)\exp(-i\omega_t\tau)\right|^2, \tag{14}$$

where we take $g(t-\tau)$ to be a Gaussian function with a width equal to the laser pulse duration. Spectrograms of the signals emitted from 5*R*, 5*Rd*, and the neat solvent, $CHCl_3$, are given in Fig. 12. The solvent behaves as an instantaneously responding medium with the time of emission determined by the optical gate of pulses 1 and 2, which arrive to the sample at the same time. It is clear from these measurements that signal emission from the solutions is delayed with respect to the neat solvent at $T=0$ fs. A positive delay in signal emis-

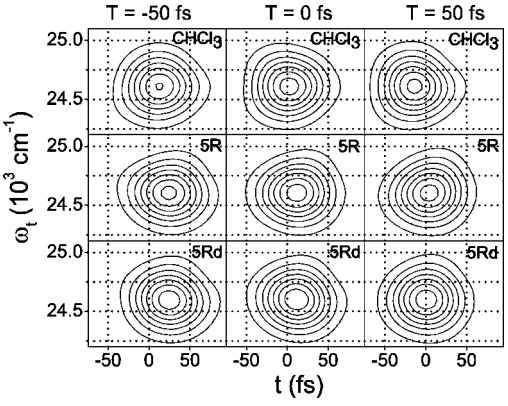

FIG. 12. Spectrograms of experimental transient grating signal pulses, Eq. (13), for the neat solvent (top), 5*R* (middle) and 5*Rd* (bottom) computed using Eq. (14). The transient grating signals were measured at $T=-50$ fs (left), $T=0$ fs (middle), and $T=+50$ fs (right).

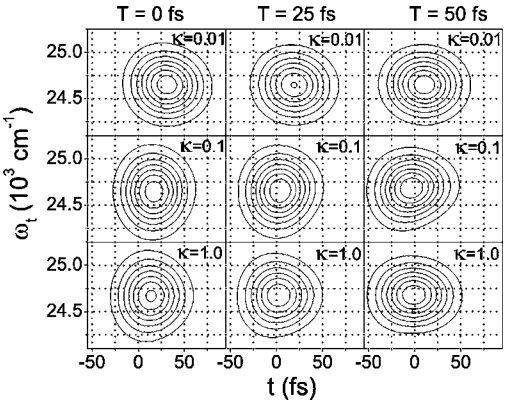

FIG. 13. Spectrograms of theoretical transient grating signal fields calculated with Eqs. (9) and (13). The form of the response function is described in Appendix C. The population time is defined by the label on top of each column. The value of the line broadening parameter, κ, is given in each panel.

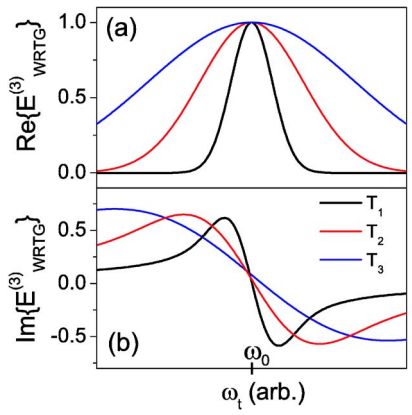

FIG. 14. Diagram for the effect of nuclear relaxation (i.e., wave packet spreading) on (a) absorptive and (b) dispersive transient grating spectra. These spectra are valid representations for experiments in which the bandwidth pulse 3 is much greater than the width of the nuclear wave packet. The absorptive part of the signal (a) is taken to be a Gaussian function and the dispersive signals (b) are given by the Kramers-Kronig transform of the functions in panel (a). T_1, T_2, and T_3 represents a population times, where $T_1<T_2<T_3$. The width of the Gaussian functions in panel (a) at T_2 and T_3 are 2.5 and 5.0 times the width of the wave packet at T_1, respectively. The shift to lower frequency (i.e., Stokes shift) which accompanies nuclear relaxation is not shown.

sion should be anticipated because a finite amount of time is required for the resonant nonlinear polarizations of $5R$ and $5Rd$ to respond to the field of pulse 3.

It was previously demonstrated with mid-infrared pulses and vibrational resonances that the temporal profile of the linear free induction decay is sensitive to line broadening mechanisms that underly the absorption spectrum.[50,81] Our measurements are sensitive to essentially the same effect (i.e., the third-order free induction decay), although in the TG experiment the resonant linewidth is dynamic in the population time T. This interpretation is made clear by numerical evaluation of Eq. (9). We have calculated transient grating signal fields using Eqs. (9) and (13) with the response function, $S(t_3,t_2,t_1)$, described in Appendix C. Calculated transient grating signal spectrograms are presented in Fig. 13 as a function of the population time T and the parameter κ, which allows for continuous interpolation between the inhomogeneous ($\kappa \ll 1$) and homogeneous limits ($\kappa \gg 1$). The calculations assume a Stokes shift of $\sim$3000 cm^{-1} (see Fig. 2), 60 fs Gaussian pulses and the pulse frequencies are taken to be equal to the absorption maximum of a two-level system. The results illustrate two important trends: the delay of emission at $T=0$ fs increases as the inhomogeneity in the linewidth increases (i.e., as κ decreases); the delay of emission decreases as the population time T increases. In other words, the time required for the nonlinear polarization to respond to pulse 3 decreases as the linewidth of the nuclear wave packet increases. The spectrograms presented in Fig. 12 are consistent with this result as they show that the resonant solutes respond more slowly than the neat solvent. In Fig. 13, the signal spectrograms calculated with $\kappa=0.1$ and $\kappa=1.0$ give similar emission times ($t \approx 15$ fs) at $T=0$ fs. However, the signal emission time converges to its asymptotic value more rapidly for $\kappa=1.0$ than for $\kappa=0.1$ as the delay, T, increases. The calculated results for $\kappa=0.1$ are most consistent with our data. The emission times for $5R$ and $5Rd$ differ by less than 2 fs for all delay times, T, with our experimental conditions. Apparently, the difference in their nuclear relaxation time scales cannot be resolved with 60 fs pulses. The theoretical calculation presented above therefore suggests that their κ's, which are on the order of 0.1, must differ by much less than an order of magnitude.

Qualitatively, the signal phase may be understood in terms of the width of a nuclear distribution of states (wave packet) and its Kramers-Kronig transform. At zero delay, the breadth of the photoexcited nuclear distribution of states resembles the homogeneous linewidth (1500–2000 cm^{-1} for similar molecules[43]), whereas after nuclear relaxation (T=several picoseconds) this distribution is as broad as the total width of the absorption and fluorescence spectra (8000–11 000 cm^{-1}); the Kramers-Kronig transform of the narrow distribution at time zero gives greater dispersion (change in phase/unit wavelength) than for a broad distribution after nuclear relaxation is complete. This idea is illustrated in Fig. 14 as plots of the Gaussian functions (meant to represent wave packets) and their Kramers-Kronig transforms. Similar information is obtained by pump-probe with a narrowband pump and dispersed broadband probe pulse (i.e., transient hole burning),[82–84] although only the absorptive component of the signal phase is measured in these experiments.

Two-dimensional photon echo (PE) spectra for $5R$ are presented in Fig. 15 at populations times, T, of 0 and 3 ps. The heterodyned wavelength resolved photon echo signal, $E^{(3)}_{WRPE}(\omega_t, T=T', \tau)$, is recorded while T is fixed and τ is varied (τ is scanned for positive and negative delays). This slice of Eq. (12) is written as

$$E^{(3)}_{WRPE}(\omega_t, T=T', \tau) = E^{(3)}_{S}(\omega_t, T=T', \tau), \tag{15}$$

where T' represents a constant value of T. The PE spectrum is given by a numerical Fourier transform of $E^{(3)}_{WRPE}(\omega_t, T=T', \tau)$ with respect to τ,

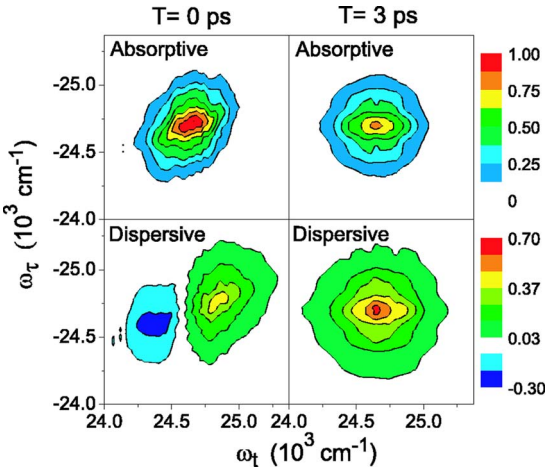

FIG. 15. Absorptive (top) and dispersive (bottom) two-dimensional photon echo spectra for $5R$ at $T=0$ ps (left) and $T=3$ ps (right). Absorptive and dispersive spectra are given by the real and imaginary parts of Eq. (16), respectively. The spectra are normalized to one so their intensities can be directly compared.

$$S_{\mathrm{PE}}(\omega_t, T=T', \omega_\tau) = \int_{-\infty}^{\infty} d\tau E^{(3)}_{\mathrm{WRPE}}(\omega_t, T=T', \tau)\exp(i\omega_\tau\tau). \tag{16}$$

The absorptive plots show the correlation between the absorbed frequency components of pulse 3, ω_t, and the initial transition dipole oscillation frequency, ω_τ. Similarly, the dispersive spectra qualitatively represent the phase shift induced at ω_t due to the absorption at ω_τ. At time zero, the absorptive spectrum is elongated with respect to the diagonal (ω_τ vs ω_t), whereas at 3 ps the peak is more symmetric. This change in line shape represents the loss in correlation for dipole oscillation frequencies (ω_τ vs ω_t) in the τ and t time intervals and is a signature that nuclear motion is frozen within the bandwidth of the laser pulse at $T=0$ ps. The dispersive PE spectra change significantly from $T=0-3$ ps population time. Positive and negative features with complicated line shapes are seen in the dispersive spectra at 0 ps, whereas the spectrum is symmetric and positive at 3 ps.

The projection-slice theorem of Fourier transforms[85] may be invoked to understand the relation between the spectra presented in Figs. 11 and 15. The absorptive and dispersive TG spectra at a population time, T', are equivalent to the projections of the corresponding PE spectra (also at $T=T'$) onto the ω_t axis. This relation is stated mathematically as[40]

$$E_{\mathrm{WRTG}}(\omega_t, T=T', \tau=0) = \frac{|\omega_t|}{n(\omega_t)}\int_{-\infty}^{\infty} S_{\mathrm{PE}}(\omega_t, T=T', \omega_\tau)d\omega_\tau. \tag{17}$$

The absolute phase of the PE spectrum is defined using Eq. (17) and in turn the phase of TG spectra are calibrated with respect to a transparent solvent. This step in calibrating the phase of the PE spectrum is necessary because spectral interferometry gives the signal phase with an unknown constant term that must be parametrized. These projections are compared in Fig. 16. The comparison of PE and TG results for $5R$ suggests that TG with dispersed heterodyned detection gives similar information to PE. In other words, the dispersion of the TG signal field at $T=0$ ps is a signature of correlated transition dipole oscillation frequencies during τ and t and that loss of this correlation due to nuclear relaxation reduces signal dispersion.

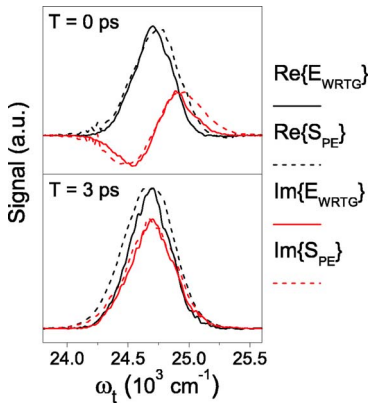

FIG. 16. Comparison of the dispersed TG spectra [Eq. (13), solid] and the projections of the real and imaginary photon echo spectra (dashed) shown in Fig. 15 onto the ω_t axis at $T=0$ and 3 ps population times. The projection is defined by Eq. (17).

IV. CONCLUSIONS

There are three main conclusions to draw from this paper. First, our anisotropy experiments and electronic structure calculations suggest that the Frenkel-exciton model for electronic structure of molecular aggregates is not appropriate for PCP-linked dimers. This is the most important conclusion in terms of the photophysical properties of these molecules. Second, the application of PE and TG spectroscopies to $5R$ and $5Rd$ has revealed that their homogeneous/inhomogeneous line broadening processes are indistinguishable with 60 fs pulses. Third, the electric field-resolved four-wave mixing measurements show that the TG signal field contains essentially the same information as the PE spectrum.

The electronic structure of $5Rd$ is not properly described with a Frenkel exciton basis consisting of only monomeric states (see Appendix A). Transient anisotropy measurements for $5Rd$ reveal a fast internal conversion between the excited states, IIa and IIb,[31] and suggest the angle between the transition dipoles connecting these states to the ground state is 50°–60°, whereas 90° is expected for degenerate basis states. Information on the angle between these transition dipoles cannot be derived from the linear absorption spectra alone; pump-probe anisotropy experiments are necessary. In addition, the transition densities of $5Rd$ do not resemble symmetric and antisymmetric combinations of monomeric excitations. This is clear by inspection of Figs. 5(a) and 5(b). Apparently, the PCP moiety is an effective conduit for electronic charge, which suggests that the orbitals of 5R subunits overlap. This conclusion is in agreement with previous work involving similar molecules in which phenyl groups are closely spaced and oriented such that their π orbitals overlap.[31,36,43,86,87] Studies of similar PCP dimers have suggested that significant through-space electrostatic coupling occurs between the monomer constituents,[35–37] which is con-

sistent with the interaction mechanism assumed in the Frenkel exciton model (Appendix A). However, the measurements presented here indicate this model is not valid for 5*Rd*. This leads us to conclude that a through-bond coupling mechanism is significant for 5*Rd*; the orbitals of the 5*R* monomer units overlap and interfere.

TG signal field emission times for 5*R* and 5*Rd* differ by less than 2 fs at all delay times, *T*. Our simulations of the TG signal fields presented in Fig. 13 suggest that their κ's (Appendix C), which are on the order of $\kappa=0.1$, differ by much less than an order of magnitude. Therefore, we conclude that the nuclear relaxation in the excited electronic states of 5*R* and 5*Rd* occurs on similar time scales. This is not obvious *a priori* and may not be a general conclusion for the PCP-linked dimers with different morphologies. The calculation shown in Fig. 6 indicates that the interactions between the 5*R* subunits in 5*Rd* results in different potential energy surfaces for the inter-ring torsional coordinates of the monomer and dimer. Thus, our field-resolved TG measurements suggest that these differences in the equilibrium geometries do not lead to energetic barriers that are sufficient to slow down the relaxation of 5*Rd* with respect to 5*R*.

Signatures of nuclear relaxation processes in four-wave mixing signal field spectrograms were previously studied theoretically.[88] However, this viewpoint has rarely been used for experimental interpretation.[54,55,89,90] Measurements and calculations presented above show that the time of signal emission contains information regarding nuclear relaxation for both the TG and PE techniques. This finding suggests that finer details of nuclear motion may be obtained by analyzing the higher order spectral phase of transient grating signal fields using broader bandwidth laser pulses. For our measurements, the TG and PE measurements are not sensitive to population dynamics because the pulse bandwidth is small compared to the energy gap ($\sim$3000 cm^{-1}) between the excited states. Future applications of field-resolved four-wave mixing techniques involving nonadiabatic processes such as chemical reactions and energy transfer[91] may reveal that PE gives unique information on the evolution of the correlation between reactant and product states during a chemical process.[92] It is important to keep in mind that this correlation cannot be fully reconstructed by conventional pump-probe experiments with tunable narrow band pump pulses and dispersed detection of a broadband probe because of the compromise that must be made between time- and spectral-resolution for the pump pulse. PE Fourier transform spectroscopy is immune to this tradeoff as there is no loss in spectral resolution for broader bandwidth (shorter) pulses. The spectral resolution is determined by the temporal length of the scan (67 cm^{-1} for 500 fs scan), but can also be zero padded along with the use of apodization functions to achieve numerical spectral resolution of less than 1 cm^{-1}.[78]

ACKNOWLEDGMENTS

This research was supported by the NSF Grant No. NIRT ERC 0303389. One of the authors (N.F.S.) acknowledges additional support by NSF (Grant No. CHE 0317009). Another author (R.A.N.) thanks CAPES/Brazil for support through a graduate research fellowship.

APPENDIX A: THE FRENKEL EXCITON MODEL

In the simplest case of a dimer composed of identical monomers, coupling between monomers results in four eigenstates. For example, the states of a two-level monomer at site α may be written $|1^\alpha\rangle$ and $|2^\alpha\rangle$. If the orbitals of a pair of monomers do not overlap (i.e., only through-space electrostatic coupling), then the states of the dimer can be described with a basis of direct product states of the individual chromophores: $|1^\alpha 1^\beta\rangle$, $|1^\alpha 2^\beta\rangle$, $|2^\alpha 1^\beta\rangle$, and $|2^\alpha 2^\beta\rangle$. The Frenkel-exciton Hamiltonian[46,47] may then be written as

$$H=\sum_{\alpha=1}^{2} E_2^\alpha |2^\alpha\rangle\langle 2^\alpha| + \sum_{\alpha>\beta} V_{1221}^{\alpha,\beta}(|1^\alpha\rangle\langle 2^\alpha|)(|2^\beta\rangle\langle 1^\beta|), \quad \text{(A1)}$$

where E_2^α is the energy difference between states 1 and 2 at site α ($E_1^\alpha=0$) and $V_{1221}^{\alpha,\beta}$ is the Coulomb coupling between the monomers. For a degenerate basis, the eigenvalues of this Hamiltonian are 0, $E_2^\alpha - V_{1221}^{\alpha,\beta}$, $E_2^\alpha + V_{1221}^{\alpha,\beta}$, and $2E_1^\alpha$. In order of increasing energy, the eigenfunctions are

$$|g\rangle = |1^\alpha 1^\beta\rangle, \quad \text{(A2a)}$$

$$|-\rangle = \frac{1}{\sqrt{2}}(|1^\alpha 2^\beta\rangle - |2^\alpha 1^\beta\rangle), \quad \text{(A2b)}$$

$$|+\rangle = \frac{1}{\sqrt{2}}(|1^\alpha 2^\beta\rangle + |2^\alpha 1^\beta\rangle), \quad \text{(A2c)}$$

$$|f\rangle = |2^\alpha 2^\beta\rangle. \quad \text{(A2d)}$$

The antisymmetric combination, $|-\rangle$, is lower in energy when $V_{1221}^{\alpha,\beta}$ is positive. An important aspect of this model is that the transition dipoles connecting the ground state to states $|-\rangle$ and $|+\rangle$ are perpendicular, a property that is experimentally accessible by pump-probe anisotropy experiments. This is shown by computing the matrix elements of the dipole operator, $\mu=\mu_{21}^\alpha|2^\alpha\rangle\langle 1^\alpha| + \mu_{21}^\beta|2^\beta\rangle\langle 1^\beta|$, in the exciton basis. The four nonzero transition dipole matrix elements are

$$\mu_{+g} = \frac{1}{\sqrt{2}}(\mu_{21}^\alpha + \mu_{21}^\beta), \quad \text{(A3a)}$$

$$\mu_{-g} = \frac{1}{\sqrt{2}}(\mu_{21}^\alpha - \mu_{21}^\beta), \quad \text{(A3b)}$$

$$\mu_{f+} = \frac{1}{\sqrt{2}}(\mu_{21}^\alpha + \mu_{21}^\beta), \quad \text{(A3c)}$$

$$\mu_{f-} = -\frac{1}{\sqrt{2}}(\mu_{21}^\alpha - \mu_{21}^\beta). \quad \text{(A3d)}$$

For a homodimer such as 5*Rd* $|\mu_{21}^\alpha| = |\mu_{21}^\beta|$. The fundamental assumption of this model is that the electronic orbitals of the monomers do not overlap. If this condition holds, then the excited states, $|-\rangle$ and $|+\rangle$, of 5*Rd* should resemble symmet-

ric and antisymmetric combinations of $5R$ excitations and must have perpendicular transition dipoles with state $|g\rangle$.

APPENDIX B: ORIENTATIONAL AVERAGES

More detail is given here on calculating the anisotropies given in Eq. (3). We use a similar notation to that given in Ref. 70, where the computation of pump-probe anisotropy is reviewed. Elements of the Euler rotation matrix, $(\hat{u}\cdot\hat{U})$, are expressed in terms of unit vectors in the molecular $\hat{u}=\hat{x},\hat{y},\hat{z}$, and laboratory frames $\hat{U}=\hat{X},\hat{Y},\hat{Z}$. If the pump and probe are taken to be polarized along the $\hat{Z}$ and $\hat{Y}$ directions, then the five fundamental orientational averages may be written as

$$\langle(\hat{x}\cdot\hat{Z})^4\rangle = 1/5, \tag{B1}$$

$$\langle(\hat{x}\cdot\hat{Z})^2(\hat{y}\cdot\hat{Y})^2\rangle = 2/15, \tag{B2}$$

$$\langle(\hat{x}\cdot\hat{Z})^2(\hat{x}\cdot\hat{Y})^2\rangle = 1/15, \tag{B3}$$

$$\langle(\hat{x}\cdot\hat{Z})(\hat{y}\cdot\hat{Z})(\hat{y}\cdot\hat{Y})(\hat{x}\cdot\hat{Y})\rangle = -1/30, \tag{B4}$$

$$\langle(\hat{x}\cdot\hat{Z})^2(\hat{x}\cdot\hat{Y})(\hat{y}\cdot\hat{Y})\rangle = 0. \tag{B5}$$

It is then possible to compute the anisotropy for any term in the response function using these averages. For example, the ESE anisotropy is found by considering two cases (see Fig. 10): μ_{ge} and $\mu_{ge'}$ are parallel; μ_{ge} and $\mu_{ge'}$ are perpendicular. For the parallel case, Equations (B1) and (B3) are equal to the *ZZZZ* and *ZZXX* tensor elements, respectively. If μ_{ge} and $\mu_{ge'}$ are perpendicular, the *ZZZZ* and *ZZXX* tensor elements are given by Eqs. (B3) and (B2), respectively. Equation (3) is a linear combination of these two cases.

APPENDIX C: NONLINEAR RESPONSE FUNCTION

Knowledge of the external electric fields and the third order impulse response function, $S(t_3,t_2,t_1)$, is required to evaluate Eq. (9). $S(t_3,t_2,t_1)$ is fully parameterized by eigenstate energies and line broadening functions corresponding to every pair of energy levels of the material system. A detailed description of the terms in $S(t_3,t_2,t_1)$ is given in Ref. 65. For our calculations, we assume a two-level system and calculate the line broadening function, $g(t)$, in the overdamped and high-temperature limits. This model is appropriate for describing solvation dynamics of a dye molecule in solution at ambient temperatures.

Under these assumptions, the line broadening function is written as[65]

$$g(t) = \frac{2\lambda k_B T}{\hbar\Lambda^2}[\exp(-\Lambda t) + \Lambda t - 1] - \frac{i\lambda}{\Lambda}[\exp(-\Lambda t) + \Lambda t - 1]. \tag{C1}$$

The parameter, Λ, represents the time-scale for fluctuations of the electronic transition energy, whereas λ is related to their magnitude, Δ. In the static limit, which is a good approximation for the systems considered in this paper, Δ is given by

$$\Delta^2 = \frac{2\lambda k_B T}{\hbar} \tag{C2}$$

and 2λ is equal to the Stokes shift. A useful feature of this model is the possibility of interpolating between the static and homogenous limits of line broadening using a single parameter, κ, which is defined by $\kappa \equiv \Lambda/\Delta$.

[1] C. A. Mirkin and M. A. Ratner, Annu. Rev. Phys. Chem. **43**, 719 (1992).
[2] T. Rueckes, K. Kim, E. Joselevich, G. Y. Tseng, C. Cheung, and C. M. Lieber, Science **289**, 94 (2000).
[3] A. R. Pease, J. O. Jeppesen, J. F. Stoddart, Y. Luo, C. P. Collier, and J. R. Heath, Acc. Chem. Res. **34**, 433 (2001).
[4] J. Cornil, D. A. dos Santos, X. Crispin, R. Silbey, and J. L. Bredas, J. Am. Chem. Soc. **120**, 1289 (1998).
[5] J. R. Sheats, H. Antoniadis, M. Hueschen, W. Leonard, J. Miller, R. Moon, and D. A. S. Roitman, Science **273**, 887 (1996).
[6] R. H. Friend, R. W. Gymer, A. B. Holmes *et al.*, Nature (London) **397**, 121 (1999).
[7] C. H. Lee, G. Yu, D. Moses, and A. J. Heeger, Synth. Met. **69**, 429 (1995).
[8] D. M. Hanson, J. Chem. Phys. **52**, 3409 (1970).
[9] Y. Yonezawa and T. Hayashi, J. Lumin. **47**, 49 (1990).
[10] S. De Boer and D. A. Wiersma, Chem. Phys. Lett. **165**, 45 (1990).
[11] V. I. Novoderezhkin and A. P. Razjivin, Chem. Phys. **211**, 211 (1996).
[12] R. Jimenez, S. E. Bradforth, and G. R. Fleming, J. Phys. Chem. B **100**, 6825 (1996).
[13] S. R. Greenfield, M. Seibert, Govindjee, and M. R. Wasielewski, Chem. Phys. **210**, 279 (1996).
[14] S. Savikhin and W. S. Struve, Chem. Phys. **210**, 91 (1996).
[15] L. A. Walker II, J. J. Shiang, N. A. Anderson, S. H. Pullen, and R. J. Sension, J. Am. Chem. Soc. **120**, 7286 (1998).
[16] V. Sundstrom, T. Pullerits, and R. van Grondelle, J. Phys. Chem. B **103**, 2327 (1999).
[17] V. Nagarajan, E. T. Johnson, J. C. Williams, and W. W. Parson, J. Phys. Chem. B **103**, 2297 (1999).
[18] L. D. Book, A. E. Ostafin, N. Ponomarenko, J. R. Norris, and N. F. Scherer, J. Phys. Chem. B **104**, 8295 (2000).
[19] J. C. Chiang and A. G. MacDiarmid, Synth. Met. **13**, 193 (1986).
[20] E. S. Maniloff, V. I. Klimov, and D. W. McBranch, Phys. Rev. B **56**, 1876 (1997).
[21] M. Wohlgenannt, W. Graupner, G. Leising, and Z. V. Vardeny, Phys. Rev. Lett. **82**, 3344 (1999).
[22] C. Gadermaier and G. Lanzani, J. Phys.: Condens. Matter **14**, 9785 (2002).
[23] D. Belijonne, G. Pourtois, C. Silva, E. Hennebicq, L. M. Herz, R. H. Friend, G. D. Scholes, S. Setayesh, K. Mullen, and J. L. Bredas, Proc. Natl. Acad. Sci. U.S.A. **99**, 10982 (2002).
[24] I. Chen, D. McBranch, H. I. Wang, R. Hegelson, F. Wudl, and D. G. Whitten, Proc. Natl. Acad. Sci. U.S.A. **96**, 12287 (1999).
[25] E. E. Jelley, Nature (London) **139**, 637 (1937).
[26] G. Scheibe, Angew. Chem. **50**, 212 (1937).
[27] A. G. MacDiarmid and A. J. Epstein, Synth. Met. **69**, 69 (1995).
[28] B. Servet, G. Horowitz, S. Ries *et al.*, Chem. Mater. **6**, 1809 (1994).
[29] A. Dodalabalapur, L. Torsi, and H. E. Katz, Science **268**, 270 (1995).
[30] G. C. Bazan, W. J. Oldham, R. J. Lachicotte, S. Tretiak, V. Chernyak, and S. Mukamel, J. Am. Chem. Soc. **120**, 9188 (1998).
[31] S. Wang, G. C. Bazan, S. Tretiak, and S. Mukamel, J. Am. Chem. Soc. **122**, 1289 (2000).
[32] J. W. Hong, H. Benmansour, and G. C. Bazan, Chem.-Eur. J. **9**, 3186 (2003).
[33] G. P. Bartholomew, M. Rumi, S. J. K. Pond, J. W. Perry, S. Tretiak, and G. C. Bazan, J. Am. Chem. Soc. **126**, 11529 (2004).
[34] E. S. Baker, J. W. Hong, J. Gidden, G. Bartholomew, G. C. Bazan, and M. T. Bowers, J. Am. Chem. Soc. **126**, 6255 (2004).
[35] G. P. Bartholomew and G. C. Bazan, J. Am. Chem. Soc. **124**, 5183 (2002).
[36] G. P. Bartholomew, G. P. Ledoux, S. Mukamel, J. Bazan, and G. C. Zyss, J. Am. Chem. Soc. **124**, 13480 (2002).

[37] J. W. Hong, H. Y. Woo, B. Liu, and G. C. Bazan, J. Am. Chem. Soc. **127**, 7435 (2005).
[38] D. J. Cram and R. H. Bauer, J. Am. Chem. Soc. **81**, 5971 (1959).
[39] F. Voegtle, *Cyclophane Chemistry* (Wiley, New York, 1993).
[40] D. M. Jonas, Annu. Rev. Phys. Chem. **54**, 425 (2003).
[41] T. Brixner, T. Mancal, I. V. Stiopkin, and G. R. Fleming, J. Chem. Phys. **121**, 4221 (2004).
[42] M. L. Cowan, J. P. Ogilvie, and R. J. D. Miller, Chem. Phys. Lett. **386**, 184 (2004).
[43] W. Leng, J. Grunden, G. P. Bartholomew, G. C. Bazan, and A. M. Kelley, J. Phys. Chem. A **108**, 10050 (2004).
[44] S. Tretiak and S. Mukamel, Chem. Rev. (Washington, D.C.) **102**, 3171 (2002).
[45] M. Pope and C. E. Swenberg, *Electronic Processes in Organic Crystals* (Oxford University Press, New York, 1982).
[46] A. Davydov, *Theory of Molecular Excitons* (Plenum, New York, 1971).
[47] V. Capek and E. Silinsh, *Organic Molecular Crystals: Interaction, Localization, and Transport Phenomena* (AIP, New York, 1994).
[48] J. K. Lee, R. R. Schrock, D. R. Baigent, and R. H. Friend, Macromolecules **28**, 1966 (1995).
[49] J. Kim, *Ultrafast Dynamics of Polarons, Excitons and Excitations in Conjugated Molecules* (Ph.D Thesis, The University of Chicago, 2004).
[50] J. A. Gruetzmacher and N. F. Scherer, Rev. Sci. Instrum. **104**, 2227 (2002).
[51] Y. H. Liau, A. N. Unterreiner, D. C. Arnett, and N. F. Scherer, Appl. Opt. **38**, 7386 (1999).
[52] C. J. Fecko, J. J. Loparo, and A. Tokmakoff, Opt. Commun. **241**, 521 (2004).
[53] L. Lepetit, G. Chéiaux, and M. Joffre, J. Opt. Soc. Am. B **12**, 2467 (1995).
[54] E. Tokunaga, A. Terasaki, and T. Kobayashi, J. Opt. Soc. Am. B **12**, 753 (1995).
[55] S. M. Gallagher, A. W. Albrecht, J. D. Hybl, B. L. Landin, B. Rajaram, and D. M. Jonas, J. Opt. Soc. Am. B **15**, 2338 (1998).
[56] C. Dorrer, N. Belabas, J. P. Likforman, and M. Joffre, J. Opt. Soc. Am. B **17**, 1795 (2000).
[57] S. Park, J. Kim, and N. F. Scherer (in preparation).
[58] S. Park, J. Kim, and N. F. Scherer, *Ultrafast Phenomena XIV* (Springer, Berlin, 2005), Vol. 79.
[59] G. D. Goodno, V. Astinov, and R. J. D. Miller, J. Phys. Chem. A **106**, 10755 (2002).
[60] Q. H. Xu, Y. Z. Ma, and G. R. Fleming, J. Phys. Chem. A **106**, 10755 (2002).
[61] T. Brixner, I. V. Stiopkin, and G. R. Fleming, Opt. Lett. **29**, 884 (2004).
[62] M. J. S. Dewar, E. G. Zoesbisch, E. F. Healy, and J. J. P. Stewart, J. Am. Chem. Soc. **107**, 3902 (1985).
[63] M. C. Zerner, G. H. Loew, R. F. Kirchner, and U. T. Mueller-Westerhoff, J. Am. Chem. Soc. **102**, 590 (1980).
[64] M. J. Frisch, G. W. Trucks, H. B. Schlegel, G. E. Scuseria, M. A. Robb, J. R. Cheeseman, and J. A. Montgomery, Jr., GAUSSIAN 03, Revision C.02 (2004).
[65] S. Mukamel, *Principles of Nonlinear Optical Spectroscopy* (Oxford University Press, New York, Oxford, 1995).
[66] R. L. Martin, J. Chem. Phys. **118**, 4775 (2003).
[67] J. M. Thijssen, *Computational Physics* (Cambridge University Press, Cambridge, UK, 2000).
[68] C. H. Choi and M. Kertesz, J. Phys. Chem. A **101**, 3823 (1997).
[69] F. Duschinskii, Acta Physicochim. URSS **7**, 551 (1937).
[70] W. Qian and D. M. Jonas, J. Chem. Phys. **119**, 1611 (2003).
[71] Y. R. Kim, P. Share, M. Pereira, M. Sarisky, and R. M. Hochstrasser, J. Chem. Phys. **91**, 7557 (1989).
[72] A. A. Ferro and D. M. Jonas, J. Chem. Phys. **115**, 6281 (2001).
[73] C. K. Min, T. Joo, M. C. Yoon, C. M. Kim, Y. N. Hwang, D. Kim, N. Aratani, N. Yoshida, and A. Osuka, J. Chem. Phys. **114**, 6750 (2001).
[74] O. P. Varnavski, J. C. Ostrowski, L. Sukhomlinova, R. J. Twieg, G. C. Bazan, and T. Goodson III, J. Am. Chem. Soc. **124**, 1736 (2002).
[75] K. Wynne and R. M. Hochstrasser, Chem. Phys. **171**, 179 (1993).
[76] R. S. Knox and D. Gülen, Photochem. Photobiol. **57**, 40 (1993).
[77] R. Trebino, *Frequency Resolved Optical Gating: The Measurement of Ultrashort Laser Pulses* (Kluwer, Boston, Dordrecht, London, 2000).
[78] M. Khalil, N. Demirdöven, and A. Tokmakoff, J. Phys. Chem. A **107**, 5258 (2003).
[79] N. Belabas and D. M. Jonas, J. Opt. Soc. Am. B **22**, 655 (2005).
[80] R. A. Altes, J. Acoust. Soc. Am. **67**, 1232 (1980).
[81] J. A. Gruetzmacher, J. Chem. Phys. **119**, 1590 (2003).
[82] C. H. Brito-Cruz, R. L. Fork, W. H. Knox, and C. V. Shank, Chem. Phys. Lett. **132**, 341 (1986).
[83] T. J. Kang, Y. Jongwan, and M. Berg, J. Chem. Phys. **94**, 2413 (1991).
[84] H. Murakami, S. Kinoshita, Y. Hirata, T. Okada, and N. Mataga, J. Chem. Phys. **97**, 7881 (1992).
[85] R. R. Ernst, G. Bodenhausen, and A. Wokaun, *Principles of Nuclear Magnetic Resonance in One and Two Dimensions* (Oxford University Press, New York, 1987).
[86] D. Belijonne, J. Comil, R. Silbey, P. Millié, and J. L. Brédas, J. Chem. Phys. **112**, 4749 (2000).
[87] A. M. Moran, G. P. Bartholomew, G. C. Bazan, and A. M. Kelley, J. Phys. Chem. A **106**, 4928 (2002).
[88] S. Mukamel, C. Ciordas-Ciudariu, and V. Khidekel, IEEE J. Quantum Electron. **32**, 1278 (1996).
[89] W. P. de Boeij, M. S. Psenichnikov, and D. A. Wiersma, Chem. Phys. Lett. **238**, 1 (1995).
[90] J. P. Likforman, M. Joffre, and V. Thierry-Mieg, Opt. Lett. **22**, 1104 (1997).
[91] T. Brixner, J. Stenger, H. M. Vaswani, M. Cho, R. E. Blankenship, and G. R. Fleming, Nature (London) **434**, 625 (2005).
[92] M. Cho, H. M. Vaswani, T. Brixner, J. Stenger, and G. R. Fleming, J. Phys. Chem. B **109**, 10542 (2005).